

<b>Title</b>	2D nanosheet paint from solvent-exfoliated Bi <sub>2</sub> Te <sub>3</sub> ink
<b>Author(s)</b>	Carroll, Elaine; Buckley, Darragh; Mogili, N. Vishnu V.; McNulty, David; Moreno, M. Sergio; Glynn, Colm; Collins, Gillian; Holmes, Justin D.; Razeeb, Kafil M.; O'Dwyer, Colm
<b>Publication date</b>	2017-08-09
<b>Original citation</b>	Carroll, E., Buckley, D., Mogili, N. V. V., McNulty, D., Moreno, M. S., Glynn, C., Collins, G., Holmes, J. D., Razeeb, K. M. and O'Dwyer, C. (2017) '2D nanosheet paint from solvent-exfoliated Bi <sub>2</sub> Te <sub>3</sub> ink', Chemistry of Materials, 29(17), pp. 7390-7400. doi:10.1021/acs.chemmater.7b02321
<b>Type of publication</b>	Article (peer-reviewed)
<b>Link to publisher's version</b>	<a href="http://dx.doi.org/10.1021/acs.chemmater.7b02321">http://dx.doi.org/10.1021/acs.chemmater.7b02321</a> Access to the full text of the published version may require a subscription.
<b>Rights</b>	© 2017 American Chemical Society. This is an open access article published under an ACS AuthorChoice License, which permits copying and redistribution of the article or any adaptations for non-commercial purposes. <a href="http://pubs.acs.org/page/policy/authorchoice_termsfuse.html">http://pubs.acs.org/page/policy/authorchoice_termsfuse.html</a>
<b>Item downloaded from</b>	<a href="http://hdl.handle.net/10468/4687">http://hdl.handle.net/10468/4687</a>

Downloaded on 2018-08-23T19:42:39Z

## 2D Nanosheet Paint from Solvent-Exfoliated $\text{Bi}_2\text{Te}_3$ Ink

Elaine Carroll,<sup>†</sup> Darragh Buckley,<sup>†</sup> N. Vishnu V. Mogili,<sup>‡</sup> David McNulty,<sup>†</sup> M. Sergio Moreno,<sup>§</sup> Colm Glynn,<sup>†</sup> Gillian Collins,<sup>†</sup> Justin D. Holmes,<sup>†,||,⊥</sup> Kafil M. Razeeb,<sup>⊥</sup> and Colm O'Dwyer<sup>\*,†,⊥</sup>

<sup>†</sup>School of Chemistry, University College Cork, Cork T12 YN60, Ireland

<sup>‡</sup>Centro Nacional de Pesquisa em Energia e Materiais (CNPEM), Brazilian Nanotechnology National Laboratory (LNNano), CEP 13083-970 Campinas/SP, Brazil

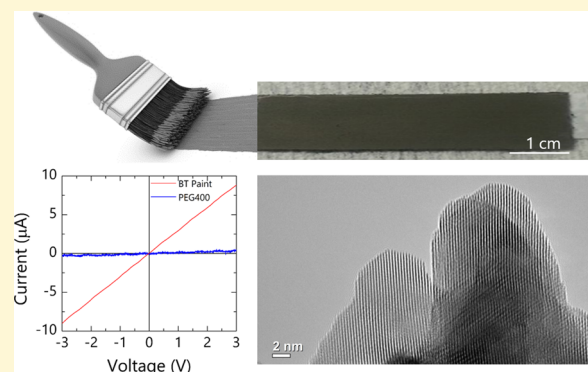
<sup>§</sup>Centro Atómico Bariloche, 8400 - S. C. de Bariloche, Argentina

<sup>||</sup>AMBER@CRANN, Trinity College Dublin, Dublin 2, Ireland

<sup>⊥</sup>Micro-Nano Systems Centre, Tyndall National Institute, Lee Maltings, Cork T12 R5CP, Ireland

### S Supporting Information

**ABSTRACT:** Embedding 2D layered materials into polymers and other materials as composites has resulted in the development of ultrasensitive pressure sensors, tunable conductive stretchable polymers, and thermoelectric coatings. As a wettable paint or ink, many 2D materials may be penciled, printed, or coated onto a range of surfaces for a variety of applications. However, the intrinsic conductive properties of painted coatings using 2D and layered materials are not completely understood, and conductive polymer additives may mask underlying properties such as directional conductivity. We report a process for making a paint from solvent-exfoliated  $\text{Bi}_2\text{Te}_3$  into solution-dispersible 2D and few-layer (multiple quintuple) nanosheet inks, that form smooth, uniform paint blends at several concentrations of  $\text{Bi}_2\text{Te}_3$ . The individual solvent-exfoliated nanosheets are edge-coated by (poly)ethylene glycol to produce a paint, stable over extended period in solution. Electrical transport is found to be sensitive to aspect ratio, and conduction along the painting direction is suppressed for longer strips so long as the aspect ratio is high (4–10× or more), but for short and wide paint strips (aspect ratio  $\leq 1$ ), conductance is improved by a factor of 3×. Square 2D paint regions show no clear directional preference for conductance at room temperature but are markedly affected by higher temperatures. Conductivity along a preferential conduction pathway through the nanosheet ensemble is modulated by 2D nanosheet stacking along the direction of paint application for a given aspect ratio. This paint and insights into geometrical 2D composite conduction may have implications for conductive composites, thermoelectrics, and writable circuits using 2D material paints or inks.



## INTRODUCTION

Basic research into two-dimensional (2D) materials, including graphene, transition metal dichalcogenides, and their carbide and carbonitride analogs such as MXenes, is progressing beyond discovery to advanced application.<sup>1–3</sup> Aside from 2D materials for use in electronics, single-molecule, submolecule, or few-molecule thick materials are being explored and optimized for significantly improved capacitive energy storage<sup>4,5</sup> and in energy harvesting, including thermoelectrics, and even ultrasensitive pressure sensors based on graphene-silly putty composites.<sup>6</sup> There is a significant need for site-specific and on demand cooling in electronic, optoelectronic, and bioanalytical devices, where cooling is currently achieved by the use of bulky and/or overdesigned system-level solutions.<sup>7,8</sup> Thermoelectric devices can address these limitations by nanostructured layered thermoelectric (TE) materials with enhanced figures of merit ( $ZT$ ). The figure of merit  $ZT =$

$S^2\sigma T/K$ , where  $S = -\Delta V/\Delta T$  is the Seebeck coefficient ( $\Delta V$  is the voltage difference caused by a temperature difference  $\Delta T$ ),  $\sigma$  is the electrical conductivity, and  $K$  is the thermal conductivity. Ideally, the  $ZT$  is maximized by processes that contribute to large electrical conductivities, while reducing or maintaining as low a thermal conductivity as possible, thus maximizing  $S$  for a high  $\sigma/K$  ratio.<sup>9–11</sup>  $\text{Bi}_2\text{Te}_3$  is of particular interest as it is both a topological insulator<sup>12,13</sup> and thermoelectric material.<sup>14</sup> Bulk  $\text{Bi}_2\text{Te}_3$  is one of the principal industrial thermoelectric materials having one of the highest thermoelectric figures of merit,  $ZT$  between 1.1 and 1.2 at room temperature.<sup>15–17</sup>

Received: June 6, 2017

Revised: August 9, 2017

Published: August 9, 2017

For electrical conductivity control, quantum confinement of charge carriers in quantum wells can lead to a considerable  $ZT$  improvement as the carrier density-of-states (DOS) near the Fermi level is boosted to increase the resultant thermopower,<sup>18,19</sup> but this depends on a material being crystalline, with thickness on the order of a few atomic layers. To fulfill these conditions, 2D materials that maintain or enhance their direct-gap semiconductivity with a high carrier density are potentially very useful. Low-dimensional structures, in principle, should also contribute the other necessary effect to increase the  $ZT$ , i.e. reduce the thermal conductivity through spatial confinement of heat-carrying acoustic phonons. At the same time, disorder can negatively affect electron mobility and affect electrical conductivity via electron scattering, thereby preventing maximum  $ZT$  enhancement. To become more useful, these layers need to be exfoliated down to smaller dimensions, such as its 2D form. Then, its thermoelectric response improves as the overall nanostructured composite approximates an electronic crystal but behaves as a phonon glass. Slowing the acoustic phonon group velocity through confinement and introducing grain boundary and point defect contacts to enhance the reduction in thermal conductivity is possible if suitable methods for 2D materials or crystallographic engineering of alloys can be developed.<sup>20</sup> Many methods have been used by others to create thin films of bismuth telluride and its related polymorphs, and a wide range of graphene-like materials and methods,<sup>21–27</sup> such as coevaporation of bismuth and of telluride<sup>28</sup> ion-beam sputtering deposition,<sup>29</sup> electrochemical deposition,<sup>30</sup> along with many more. The method that interested us was chemical exfoliation due to the recent advances in this area for high-throughput and high-quality dispersions of graphene and related 2D transition metal dichalcogenides (TMDs), for example.<sup>2,3,31,32</sup> Being able to apply this material to almost any surface or shape was explored in this work, to use sheering of 2D layers similar to solid lubricants, such as graphite/graphene<sup>33</sup> or MoS<sub>2</sub>, to affect the directional control over electrical connectivity and conductive pathways.<sup>34</sup> Advances are being made currently<sup>35</sup> in thermoelectric composites and 2D material–polymer mixtures for a range of uses, and combining 2D crystal of a material with the highest  $ZT$ , as a paint, is a promising development. Since the phonon scattering mechanisms are established for some low-dimensional materials, methods to create functional materials and coatings using such structure, while maintaining or routing electrical conductivity, are important in thermoelectrics. Most recently, a thermoelectric paint using molecular Sb<sub>2</sub>Te chalcogenidometalate was used to help sinter thermoelectric particles, achieving high thermopower output when painted onto surfaces such as p–n junction devices.<sup>36</sup>

Here, we demonstrate a method whereby optimized solvent exfoliation of Bi<sub>2</sub>Te<sub>3</sub> into solution-dispersible 2D nanosheets can form a practical thin film paint when fashioned into a smooth, uniform composite once the 2D material surface is PEGylated with (poly)ethylene glycol (PEG-400), limiting restacking/agglomeration in solution. The result is a soluble 2D Bi<sub>2</sub>Te<sub>3</sub> paint, that can be painted onto most surfaces. Atomic force microscopy, transmission electron spectroscopy, Raman spectroscopy, and scanning electron spectroscopy show that the 2D Bi<sub>2</sub>Te<sub>3</sub> material is uniformly dispersed by brush painting, forming a coherent (nonsegregated or clumpy) film. Electrical transport studies confirm that the films are conductive. By using a nonconductive binding polymer (PEG400) added to the solution to PEGylate the nanosheet and few quintuple layer

surfaces, the nature of the electron transport pathways in a range of paints with different aspect ratios (A.R.) but identical brushstrokes (direction of painting) was determined. Our work demonstrates that the paint conductance at high fill fractions of exfoliated nanosheets is controlled by the A.R. along the painting direction. The lowest conductance occurs for long, narrow painted strips. Conductance increases as length is reduced as expected, but as the A.R. approached 1 (or less), the width perpendicular to the brush stroke provides conduction pathways that markedly enhance conductivity compared to similarly short but narrow paint strips. Wider strips for a fixed length increase conductance, and this is consistent for different 2D nanosheet fill fractions, and also as a function of temperature. This 2D nanosheet paint, and new physical insights into the correlation between paint application and its conductance, has scope for diverse surface coating as a cohesive and conductive thin film (when conducting polymers are used) particularly for higher  $ZT$  materials for flexible or uniquely shaped energy harvesting or thermoelectric applications. It may also be applicable in general to solvent-exfoliated 2D materials for a range of uses from printable, flexible large area electronics to composite coatings with chemical, catalytic, or other activity and for pencilling, writing, or painting of 2D nanosheet composites for writable circuitry on plastics or nonplanar substrates.

## ■ EXPERIMENTAL SECTION

**Preparation of 2D Bi<sub>2</sub>Te<sub>3</sub> Nanosheet Dispersions.** Bismuth(III) telluride (Bi<sub>2</sub>Te<sub>3</sub>) powder, isopropyl alcohol (IPA), NMP, and/or CHP were used. All materials were purchased from Sigma-Aldrich and used as supplied. Bi<sub>2</sub>Te<sub>3</sub>, NMP/CHP, and IPA were added to a round bottomed flask in varying ratios of 1:2:15 (v/w/v) (1:1:15/2:1:15); heat was then supplied (423 K) and the mixture was refluxed for 6 h under stirring. It was then allowed to cool for ~1 h, and was and subsequently distilled for 24 h.

**Processing of 2D Bi<sub>2</sub>Te<sub>3</sub> Ink and Paint.** 2D Bi<sub>2</sub>Te<sub>3</sub> nanosheet dispersions were created using either 1-cyclohexenyl pyrrolidine (CHP) or *N*-methyl-2-pyrrolidone (NMP) as solvents. Sonication was performed for 800 min to obtain the dispersions. After the preparatory distillation step and sonication, polyethylene glycol (PEG,  $M_w = 400$  g/mol) was added to each mixture and subsequently allowed to cool while being stirred continuously for 60 min. The mixtures were then sonicated for 90 min. The 2D Bi<sub>2</sub>Te<sub>3</sub> solution was then centrifuged at 4500 rpm for 45 min. For each nanosheet dispersion, the supernatant was removed and the mixture was then painted onto substrates (glass, Si and SiO<sub>2</sub>) of known areas. The material was distributed evenly across the glass slides in predetermined A.R.s that allow examination of length/width dependence. The substrates were then dried at 100 °C for 3 h.

**Characterization Methods.** Transmission electron microscopy (TEM) was performed using a JEOL 2100 at 200 kV. Energy-filtered TEM characterization was performed using a JEOL 2100F TEM equipped with field emission gun and Gatan Tridiem Imaging filter model 863 operating at an accelerating voltage of 200 kV. Depending upon the characterization requirement, the microscope was operated both in Conventional TEM (CTEM) and Scanning TEM (STEM) modes. The CTEM mode of operation was primarily used for selected area electron diffraction (SAED), high-resolution and energy filtered (EFTEM) imaging, while STEM was used for high-angle annular dark field (HAADF) and spectrum imaging. All the chemical characterization was performed using electron energy loss spectroscopy (EELS) technique in CTEM and STEM mode of operations. The microscope was set to have a convergence and collection angles of 15.7 and 22.35 mrad respectively and an energy spread of 0.9 eV full width at half-maximum (fwhm) for the zero-loss peak. Unfiltered and zero loss images were acquired using a 10 eV energy slit and subsequent relative thickness ( $t/\lambda$ ) maps were generated from the electron mean free path

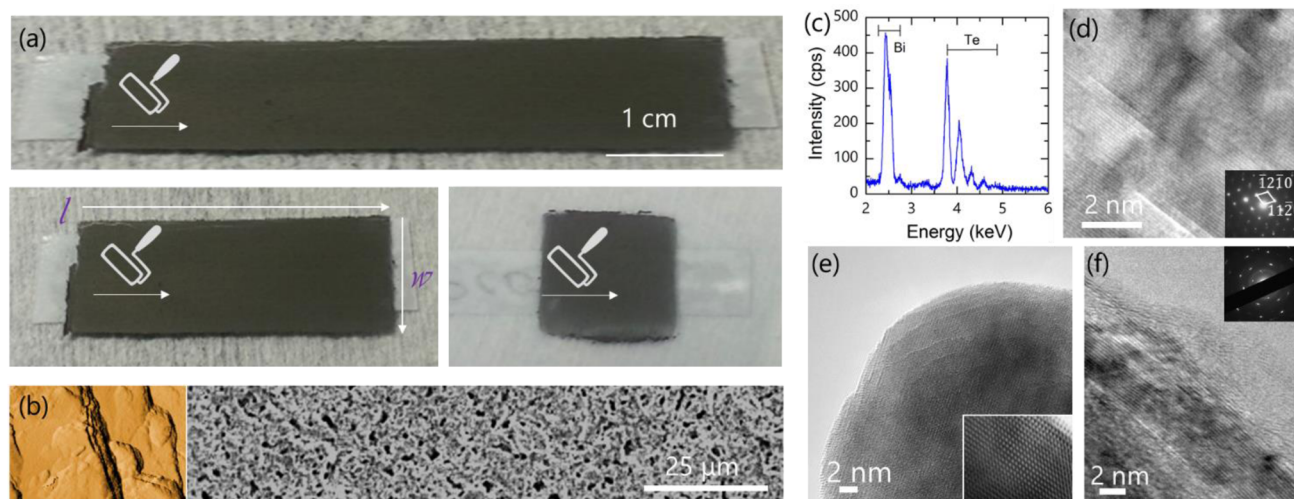


**Figure 1.** (a) Optical images of the 2D  $\text{Bi}_2\text{Te}_3$  paint on glass. The lengths ( $l$ ) of the strips are  $\sim 5$  cm, 2.5 cm, and 1 cm. A.R. =  $l \times w$ . (b) AFM images of starting  $\text{Bi}_2\text{Te}_3$  prior to exfoliation and SEM image of the surface morphology of the dried paint. (c) EDX analysis of the exfoliated nanosheet composition. (d) HRTEM image of the plan-view structure of the restacked composite layered structure of the 2D  $\text{Bi}_2\text{Te}_3$ . (Inset) Corresponding SAED pattern acquired along the  $[01-10]$  zone axis. (e) HRTEM images of individual 2D and few-layered  $\text{Bi}_2\text{Te}_3$  nanosheets with inset ED pattern, and (f) of PEG-coated few QL nanosheets.

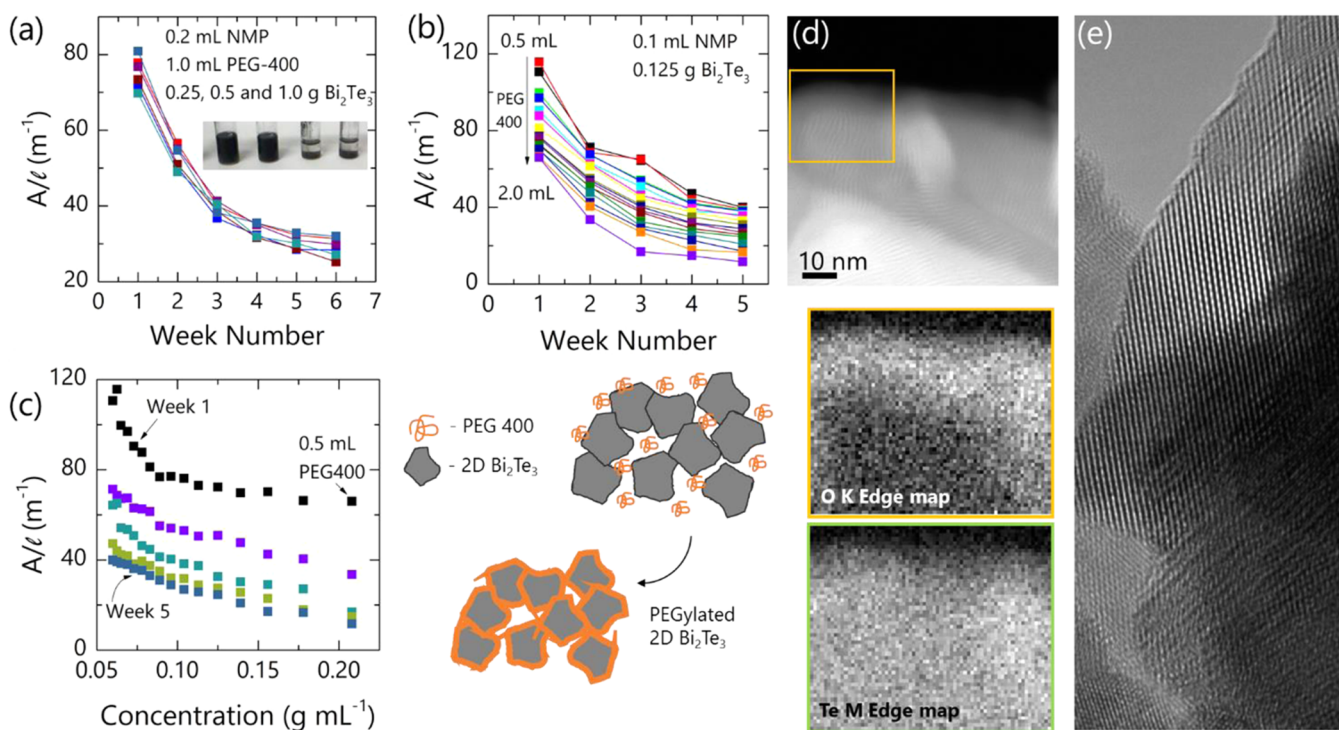


**Figure 2.** (a) Optical transmittance at  $\lambda = 532$  nm of 2D  $\text{Bi}_2\text{Te}_3$  suspensions in 0.2 mL of NMP + 1.0 mL of PEG monitored over a 6-week period. Two separate suspensions (6 solutions overall) were measured for each mass (0.25, 0.5, and 1.0 g) of  $\text{Bi}_2\text{Te}_3$ . Inset: Photograph of a typical 2D  $\text{Bi}_2\text{Te}_3$  suspension. (b) Optical transmittance of 0.125 g of 2D  $\text{Bi}_2\text{Te}_3$  suspensions in 0.1 mL of NMP over a 5-week period with different volume additions of PEG (0.5–2.0 mL). (c) Transmittance data from (b) plotted as a function of 2D  $\text{Bi}_2\text{Te}_3$  concentration in NMP with incremental increase in PEG volume. (d) Electron energy loss mapping of the O K-edge and Te M-edge and corresponding HAADF STEM image of the few QL  $\text{Bi}_2\text{Te}_3$  nanosheets. (e) HRTEM image of 2D  $\text{Bi}_2\text{Te}_3$  prior to PEG addition.

estimation. Scanning electron microscopy (SEM) was carried out with a Hitachi S4800 FESEM and FEI Quanta 650 FEG high-resolution SEM equipped with an Oxford Instruments X-MAX 20 large area Si diffused EDX detector. Images were collected at operating voltages of 10–20 kV. Attenuated total reflection Fourier-transform infrared (FTIR) spectroscopy was performed on a Nicolet 6700 FTIR. Thermogravimetric analysis (TGA) was carried out using a Mettler Toledo TGA/DSC 1 STARe System in air to replicate temperature-

dependent measurements of painted films. Raman scattering measurements were acquired using a Renishaw InVia Raman spectrometer using a 514 nm 30 mW  $\text{Ar}^+$  laser. Spectra were collected using a RenCam CCD camera. Electrical conductivity measurements were conducted in 2-probe geometry using tungsten probes and In–Ga eutectic metal contacts using either a Biologic SP150 potenti/galvanostat or a Keithley 2612B SourceMeter. Conductivity derived from ohmic response I–V curves is plotted as conductance which here

we define as conductivity as a function of the length ( $l$ ) along the painted direction. To determine the degree of solubility of 2D Bi<sub>2</sub>Te<sub>3</sub> in NMP mixed with PEG400, we measured the variation in total transmittance of a Laser Quantum GEM DPSS single transverse mode c.w. green laser emitting at  $\lambda = 532$  nm, through each solution of 2D Bi<sub>2</sub>Te<sub>3</sub>, NMP and PEG (see figure captions) in a cuvette with a 1 cm optical path length. Spectra were acquired over a sedimentation period of 6 weeks, and also re-examined after a period of 1 year to confirm solution stability.

## RESULTS AND DISCUSSION

After solvent exfoliation the 2D and few quintuple layer (QL) Bi<sub>2</sub>Te<sub>3</sub> flakes retain the crystallinity of the parent crystal. Solutions of exfoliated 2D Bi<sub>2</sub>Te<sub>3</sub> form a paint with the addition of PEG-400 (see Experimental Section and Figure 1(a)) and can be painted across a surface using a standard fine haired brush. Optical images in Figure 1(a) show various examples of low and high-A.R. strips painted in one direction. The dried paint comprises densely stacked 2D and few QL layer sheets in a partially porous (Figure 1(b)) but consistent morphology. Stoichiometric Bi<sub>2</sub>Te<sub>3</sub> composition was confirmed by EDS (Figure 1(c)) over large (several mm<sup>2</sup>) areas. AFM imaging of scored films gave an estimate of 4–5  $\mu\text{m}$  thickness; see Figure S1.

The lattice-resolved HRTEM image in Figure 1(d) confirms the identical crystal structure of the 2D nanosheets. In regions where thickness contrast is evident, and Moiré fringing from restacked nanosheets can be seen in the thicker regions and throughout this composite, overlapping sheets postsonication and mixing are common.

Exfoliation of nanosheets provides single 2D sheets and few QL crystals. Once painted, the nanosheet thickness is several molecular layers (quasi-2D) in regions—all nanosheets exhibit identical crystal structure with no in-plane defects, kinks, or layer-on-layer mismatch or changes in registry where more than one molecular layer is present. HRTEM examination in Figure 1(e) shows a lattice resolved image of a few QL Bi<sub>2</sub>Te<sub>3</sub> flakes comprising the (111) and (011) planes of Bi<sub>2</sub>Te<sub>3</sub> with the rhombohedral  $R\bar{3}m$  space group with  $D_{3d}^5$  point symmetry. The few QL and 2D nanosheet stacks within the composite are PEGylated and encapsulated in a very thin ( $\sim 2$  nm) outer surface coating of PEG (Figure 1(f)).

The solution exfoliation of graphene using *N*-methyl-2-pyrrolidone (NMP) and related methods for transition metal dichalcogenides (TMDs) and 2D materials in general is now well established.<sup>31</sup> In our 2D ink, we investigated the “shelf life” of the 2D Bi<sub>2</sub>Te<sub>3</sub> nanosheet dispersion over a 6-week period, as a function of solvent volume, PEG-400 volume addition, and the soluble Bi<sub>2</sub>Te<sub>3</sub> concentration, in Figure 2. After exfoliation and sonication, solutions are uniform dark suspensions (see Figure 2(a) inset). The optical transmittance at  $\lambda = 532$  nm was monitored over 6 weeks, and 2D Bi<sub>2</sub>Te<sub>3</sub> suspensions remain well dispersed in solutions of solvent and PEG at concentrations as high as 830 mg mL<sup>-1</sup>. The spectral absorption of the suspension measured separately was consistent as a function of wavelength in the visible range, as Bi<sub>2</sub>Te<sub>3</sub> band-edge absorption is in the far-IR region reported in the range 0.13–0.21 eV ( $\sim 6$ – $9$   $\mu\text{m}$ ).<sup>37</sup> Typical graphene suspension concentrations are of the order of  $\mu\text{g mL}^{-1}$  but remain in suspension for longer periods.<sup>2</sup> In our case, no agglomerates were found necessary to centrifuge out from the suspension.

The mild settling approaches 30% (decrease in absorbance) over 6 weeks (Figure 2(a) and Figure S2 for each

concentration, measured for two separate suspensions in each case). Concentrations in the range 0.06–0.288 kg dm<sup>-3</sup> (using 1 and 4 kg dm<sup>-3</sup> of Bi<sub>2</sub>Te<sub>3</sub> with subsequent dilution) are shown in Figure 2(b), where the PEG content was increased in 0.1 mL increments to separate solutions of 0.125 g of Bi<sub>2</sub>Te<sub>3</sub> sonicated and exfoliated in NMP, and the suspension remains dense over 6 weeks. Overall, 0.5 mL of PEG reduces settling by 10% in the first week but results in an absorbance decrease of 60 m<sup>-1</sup> (30% transmittance) increase of 5 weeks. With a monotonic (0.1 mL) increase in PEG volume for a consistent Bi<sub>2</sub>Te<sub>3</sub> and NMP concentration, it has the most significant effect on the 2D nanosheet dispersion, causing faster settling due to surface PEGylation and thus an increase in weight of the nanosheets and reduced overall solubility in NMP. Overall suspension density (absorbance) is similar for exfoliated masses of 0.125 and 1.0 g of Bi<sub>2</sub>Te<sub>3</sub> with similar PEG and NMP volumes (Figure 2(a)). The sonication and exfoliation produce high yields of 2D and few QL Bi<sub>2</sub>Te<sub>3</sub> with PEG as a paint that is stable for useful periods of time, and the suspension is reformed when resonicated. When the volume of PEG in the paint is increased, the suspension stability is consistent across a 5-week period, particularly at a higher Bi<sub>2</sub>Te<sub>3</sub> concentration (Figure 2(c)). After 5 weeks, the sedimentation rate occurs more rapidly with higher volume fractions of PEG-400 in the solution. In Figure 2(c), this solvent–polymer solution of 2D Bi<sub>2</sub>Te<sub>3</sub> shows a reduction rate in absorbance at higher concentrations, after the first week and up to 5 weeks. The absorbance difference corresponds to the sedimentation observed in Figure 2(b).

Unlike standard solvent exfoliation methods for high-yield production of 2D graphene and TMDs, for example, relatively few studies have developed exfoliation protocols for Bi<sub>2</sub>Te<sub>3</sub>. In Figure 2, we prove that soluble polymer addition does not result in agglomeration of 2D nanosheets in suspension and the solid does not crash out of solution—rather, the absorbance shown for each week in Figure 2(c) shows remarkable stability, week after week.

We observe that PEG volumes of 1.3 mL or greater in this solution markedly improve colloidal stability as measured by absorbance. At higher PEG volume addition to the solution, the stability of 2D Bi<sub>2</sub>Te<sub>3</sub> dispersion improves from 75 to 115 m<sup>-1</sup> in absorbance. Normally, dispersion of 2D materials in solvents postexfoliation follows a Beer–Lambert absorbance profile with increase in concentration. This is observed in our case also for a fixed volume and various nanosheet concentration. As a paint solution, however, the experiment in Figure 2 demonstrates that for a fixed 2D material concentration in NMP solvent, successive addition of PEG after solvent exfoliation by sonication improves colloidal stability and dispersion in solution—the concentration change includes the additional PEG volume. Electron energy loss spectroscopic mapping of the O K and Te M edges was also acquired to confirm the coating of the nanosheet and few QL structures. The STEM HAADF image and energy loss mapping confirm site specific O presence (Figure 2(d)) at the edges after sonication/exfoliation with PEG addition. The O from the poly(ethylene oxide) (PEG) in this case coats the nanosheets preferentially at the outer edges, which as HRTEM data in Figure 2(e) confirms, were unaffected by the procedure prior to PEG addition and subsequent sonication.

We then isolated and separated individual nanosheets to examine the crystal quality, composition, and PEGylation. The reduced thermal conductivity by crystalline anharmonicity<sup>38</sup> to

a lower but finite value (avoiding infinite values associated with divergence in a true 2D material), variations in the thickness of super- and submonolayer 2D nanosheets would be advantageous for suppressing heat conduction, and for high-volume-fraction addition to various composites. Few QL and submolecular layer thickness sheets could also alter topological insulating properties by redefining the surface states of the material.<sup>12,39</sup> Ideally, these effects could be facilitated by inhomogeneous exfoliation from bulk where thicknesses less than and greater than a single molecule are possible within the same nanosheet, possibly through bottom up synthetic methods.<sup>40</sup> Subsequent restacking or electrical connection, and how the paint application affects directionality of conductivity, is unexplored for 2D material of Bi<sub>2</sub>Te<sub>3</sub> and related topological insulators.

To examine and compare the 2D or few QL nature of the Bi<sub>2</sub>Te<sub>3</sub> nanosheets in the paint after exfoliation with 1-cyclohexenyl pyrrolidine (CHP) or *N*-methylpyrrolidone (NMP) solvents, Raman scattering measurements were acquired and shown in Figure 3(a) and 3(b). Raman scattering that convolutes the 2-fold degenerate E<sub>g</sub> and A<sub>1g</sub> optical phonon modes is sensitive to variations in thickness caused by reduction from 3D to 2D (single molecule thickness).<sup>41–43</sup> The bulk material exhibits two main modes: E<sub>g</sub><sup>2</sup> and the A<sub>1g</sub><sup>2</sup> in-

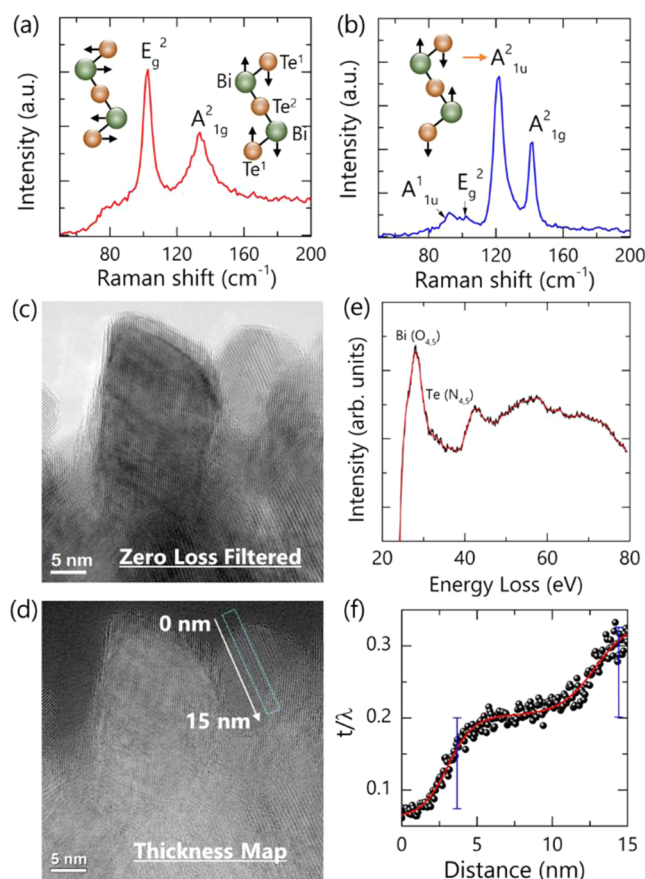


**Figure 3.** (a) Raman scattering spectra of CHP-exfoliated and (b) NMP-exfoliated 2D and few QL Bi<sub>2</sub>Te<sub>3</sub> nanosheet paint. (c) Zero-loss HRTEM image of a few QL Bi<sub>2</sub>Te<sub>3</sub> nanosheet paint flake and (d) corresponding jump-ratio thickness map image. (e) Core-loss EELS spectrum of the nanosheets and (f) corresponding log-ratio plot of thickness variations measured across the area and direction marked in (d) comprising two 2D sheets partially overlapped.

plane phonons. After exfoliation in NMP, the 2D sheets maintain a similar frequency for in-plane E<sub>g</sub><sup>2</sup> phonons, but the A<sub>1g</sub><sup>2</sup> is shifted slightly and displays a narrower fwhm. The A<sub>1g</sub><sup>2</sup> is peculiar for the Bi<sub>2</sub>Te<sub>3</sub> system as this phonon dispersion is nonmonotonic, and from 2D confinement, these phonons (with nonzero wavevectors) may have frequencies higher or lower than the Brillouin zone center.<sup>44</sup> As such, we cautiously assign this fwhm variation to a reduction in thickness toward a single molecular layer. However, this vibrational mode does not include interactions between terminating Te<sup>1</sup>–Be<sup>---</sup> of two quintuple molecular layers, making assignment to 2D or sub-2D thickness inconclusive.

Exfoliated nanosheets with single molecular layer thickness, i.e. 2D or possibly thinner (3.045 nm corresponding to the Te<sup>(1)</sup>–Bi–Te<sup>(2)</sup>–Bi–Te<sup>(1)</sup> quintuple),<sup>45</sup> can allow IR active out of plane modes to become active, as a signature of reduced dimensions for this quintuple molecular layer.

The intensity of the Raman tensor for out-of-plane A<sub>1u</sub> modes increases significantly because of inversion symmetry breaking, and this is a signature of crystallographic phonon confinement that allows IR-active modes to be seen in our 2D Bi<sub>2</sub>Te<sub>3</sub>, as it has in some other 2D TMDs, for example,<sup>46</sup> that exhibit nonlinear optical properties and valley polarization.<sup>47</sup> This IR-active phonon mode has been observed in mechanically isolated 2D sheets of Bi<sub>2</sub>Te<sub>3</sub><sup>48</sup> and hexagonal nanoplates by vapor transport using Bi<sub>2</sub>Te<sub>3</sub> powder,<sup>49</sup> and also from Bi<sub>2</sub>Te<sub>3</sub> from solvothermal growth using Bi<sub>2</sub>O<sub>3</sub> as the Bi source.<sup>50</sup> We observe this mode as the highest intensity phonon mode in Figure 3(b). Exfoliated 2D Bi<sub>2</sub>Te<sub>3</sub> is typically described as being 3D, quasi-2D (several multiple of one molecular layer), or 2D. Bulk as-received Bi<sub>2</sub>Te<sub>3</sub> and CHP-exfoliated materials show no obvious confinement effect on Raman intensity or the emergence of A<sub>1u</sub> modes (Figure 3(a)). The I(A<sub>1g</sub><sup>2</sup>)/I(E<sub>2g</sub>) intensity ratio is 0.62 (bulk is ~0.6). CHP exfoliated sheets are not reduced to 2D thickness even after extended processing.<sup>2,3</sup> NMP-exfoliated nanosheets exhibit characteristic 2D spectra, with dominant symmetry breaking in acoustic phonon modes—the A<sub>1u</sub> phonon mode is observed together with a suppression in the E<sub>2g</sub> mode intensity, and a corresponding integrated ratio as high as I(A<sub>1g</sub><sup>2</sup>)/I(E<sub>2g</sub>) = 4.2 is measured. Even after mechanical sonication, chemical exfoliation, PEGylation, filtering, and drying, the phonon features remain robust.

Importantly, these signatures evidence 2D Bi<sub>2</sub>Te<sub>2</sub> from exfoliation in NMP, PEGylated by solubilization with PEG 400 from the entire centrifuged mass, not only the more disperse, filtered supernatant. The addition of the polymer binds the nanosheets into restacked mismatched superlattice arrangements, as evident from HRTEM data in Figure 1.<sup>40,51–54</sup> We obtained additional scanning transmission electron microscopy (STEM) in high-angle annular dark field configuration (HAADF) and high-resolution TEM (HRTEM) combined with electron energy loss spectroscopy analysis (EELS). In Figure 3(c), we show a zero-loss filtered (10 eV window excluding inelastically scattered electrons) lattice-resolved HRTEM image of few 2D layer stacks. Figure 3(d) together with the thickness map based on elastic mean free path determination to obtain relative thickness differences. The low-loss EELS spectrum in Figure 3(e) of Bi O<sub>4.5</sub> and Te N<sub>4.5</sub> in tandem with selected area electron diffraction measurements across the sample (see Figure S4 for details, and Figure S5 for EELS low-loss spectrum processing) confirms stoichiometric rhombohedral Bi<sub>2</sub>Te<sub>3</sub>. Correspondingly, restacked few QL

nanosheets can be directly observed from the log-ratio plot in Figure 3(f) from a distribution in inelastic scattering events per electron ( $t/\lambda$ ), identifying individual 2D sheets overlapped in projection.

Individual few QL flakes of the solution-processed, exfoliated nanosheet flakes were also examined by EELS. From the HAADF STEM image in Figure 4(a), core-loss spectra were

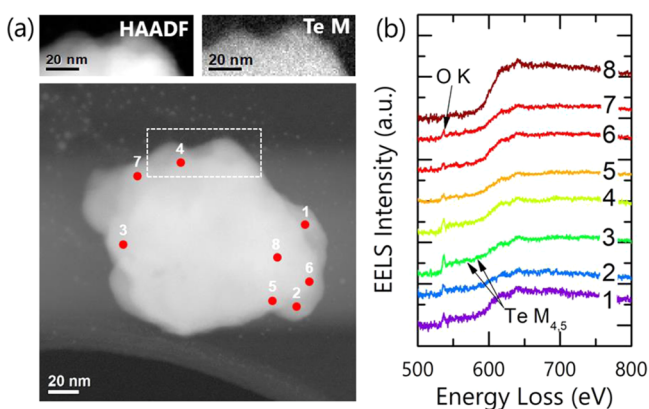


**Figure 4.** (a) High-angle annular dark field STEM image and corresponding Te M-edge electron energy loss map from the primary STEM image underneath of a few-QL flake of the  $\text{Bi}_2\text{Te}_3$  paint material. (b) Core-loss EELS spectra of O K and Te  $M_{4,5}$  edges acquired from the 8 spots indicated in (a) probing the inner surface and the outer edge regions of solution-processed  $\text{Bi}_2\text{Te}_3$  material. The spectra were background subtracted using a width of 49.2 eV between 476.8 and 526 eV.

acquired from 8 spots around the edges and also at a near-central region. The spectra in Figure 4(b) confirm that processed  $\text{Bi}_2\text{Te}_3$  retains the composition and electronic structure of the bulk material in central regions, and the Oxygen K-edge peak at  $\sim 537$  eV is localized to edge regions following functionalization and interaction with PEG. Away from the edges, no appreciable O content is found.

Electrically conductive materials with reduced thermal conductivity can be made so that phonons are confined and scattered. Such thermoelectric paints should retain good electrical conductivity without significant electron specific heat. With 2D materials in a paintable format, it is not known if a directional conductivity (regardless of fill fraction) is likely, and if this effects results from the direction of paint application for any A.R. This also applies to applications where electronic conduction is necessary or needs to be well-defined. While a conductive polymer that facilitates smooth, wettable paint to a surface and ensures the highest overall composite conductivity is useful, we chose to determine any influence on conductivity from high-fill-fraction 2D nanosheet orientation of applied paint A.R. using the PEG that helped maintain a stable disperse colloid. The addition of PEG to the bulklike 2D nanosheet dispersion in both NMP and CHP created a smooth paintable film that uniformly coated various substrates, as shown back in Figure 1 and also in Figure S3. The internal structure of the paint from exfoliation in NMP shows layer upon layer of nanosheets, some microns in length, stacked on top of one another without epitaxial arrangement of layer-by-layer order in the restacking—the microscopy examination appeared to show a random orientation of flakes that did not have a consistent flake size or shape. Preferential granular texture analysis via X-ray diffraction also proved inconclusive in

relating a specific crystallographic orientation to the painting direction. The  $\text{Bi}_2\text{Te}_3$  paint after exfoliation and processing in CHP shows larger clumps (Figure S6), consistent with Raman evidence of more bulklike structure—we observe larger grains and few grain boundaries throughout the paint. The sheared and restacked NMP-exfoliated nanosheets after painting retain their nanostructure. Upon mixing with PEG, intercalation of PEG in a manner similar to organic molecules intercalated within  $\text{V}_2\text{O}_5$  using primary alkanes or PEG, is not found.<sup>55–59</sup> Instead, the few-layer and 2D nanosheet crystals are encapsulated by a thin layer of PEG in sectional TEM images in Figure 1(f). We believe that nanosheet alignment along the painting direction is facilitated mechanically, but sheet-on-sheet assembly is a noncovalent contact of PEG-coated 2D and few QL sheets in the assembly (separated by polymer) during the painting process. The result is relatively uniform and avoids the formation of nanosheet clumps separated by domains of polymer. We propose this is feasible as the low-m.w. PEG effectively coats the outer edges of the sheets rather than forming a material-polymer mixture. In CHP, the clumps we observed in Figure S6 are due to inefficient exfoliation of source material after sonication. We suggest this process is feasible (see below) as long as there is enough polymer to provide effective separation of the nanosheets.

Inside the painted strips, microscopy examination shows the granular morphology comprises irregularly sized grains of exfoliated and restacked 2D and few-QL sheets, often overlapping. HRTEM examination of manually exfoliated paint material confirms crystalline 2D and few-QL stacks throughout. Electrical transport measurements in Figure 5(b) show that the painted thin films are ohmically conductive, and grain boundary-like intersheet contacts dominate over the free carrier conductivity of a bulk  $\text{Bi}_2\text{Te}_3$  ( $\sim 10^3$  S  $\text{cm}^{-1}$ ). The conductivity of a painted thin film of PEG is just  $\sim 6$  pS  $\text{cm}^{-1}$ . The observation of a current through the 2D  $\text{Bi}_2\text{Te}_3$ –PEG composite paint confirms the restacked  $\text{Bi}_2\text{Te}_3$  nanosheets are interconnected and electrically bridge the conduction pathways around the nonconductive host polymer coatings. The conductivity of the nanosheet paint is  $\sim 0.2$   $\mu\text{S cm}^{-1}$ , and the value is low due to the density of grain boundaries in a nominally low-conductivity material. In polycrystalline graphene by comparison, better intergrain connectivity improves in-plane conductivity by over an order of magnitude in a 2D deposit,<sup>60</sup> but high-volume-fraction composites are more resistive when calendared onto a surface; flake orientation by mechanical shearing during painting has not been examined.

This paint has a high 2D  $\text{Bi}_2\text{Te}_3$  “filler” content in a polymer matrix that is the coating on the  $\text{Bi}_2\text{Te}_3$  between grains and overlapping 2D nanosheets. As such, the conductivity of the 2D  $\text{Bi}_2\text{Te}_3$  should be an upper bound; a reduction in 2D material content (and increase in polymer content) would reduce the conductivity significantly following known mixture rules for percolating electronic conductivity in polymer–material composites.<sup>4,34,61,62</sup> We examined the effect of  $\text{Bi}_2\text{Te}_3$  nanosheet reduction (but at concentrations that retain a high enough volume fraction to avoid strong percolating dependence).

In dc  $I$ – $V$  measurements in Figure 5, we consistently observe an ohmic response from the 2D  $\text{Bi}_2\text{Te}_3$  paint at both concentrations. The filling fractions of the high (4 kg  $\text{dm}^{-3}$ ) and low (1 kg  $\text{dm}^{-3}$ )  $\text{Bi}_2\text{Te}_3$  are far above what is considered to be the coagulation threshold in extruded, melt, or similar composites. Even for few QL  $\text{Bi}_2\text{Te}_3$  sheets of 1–3 nm in

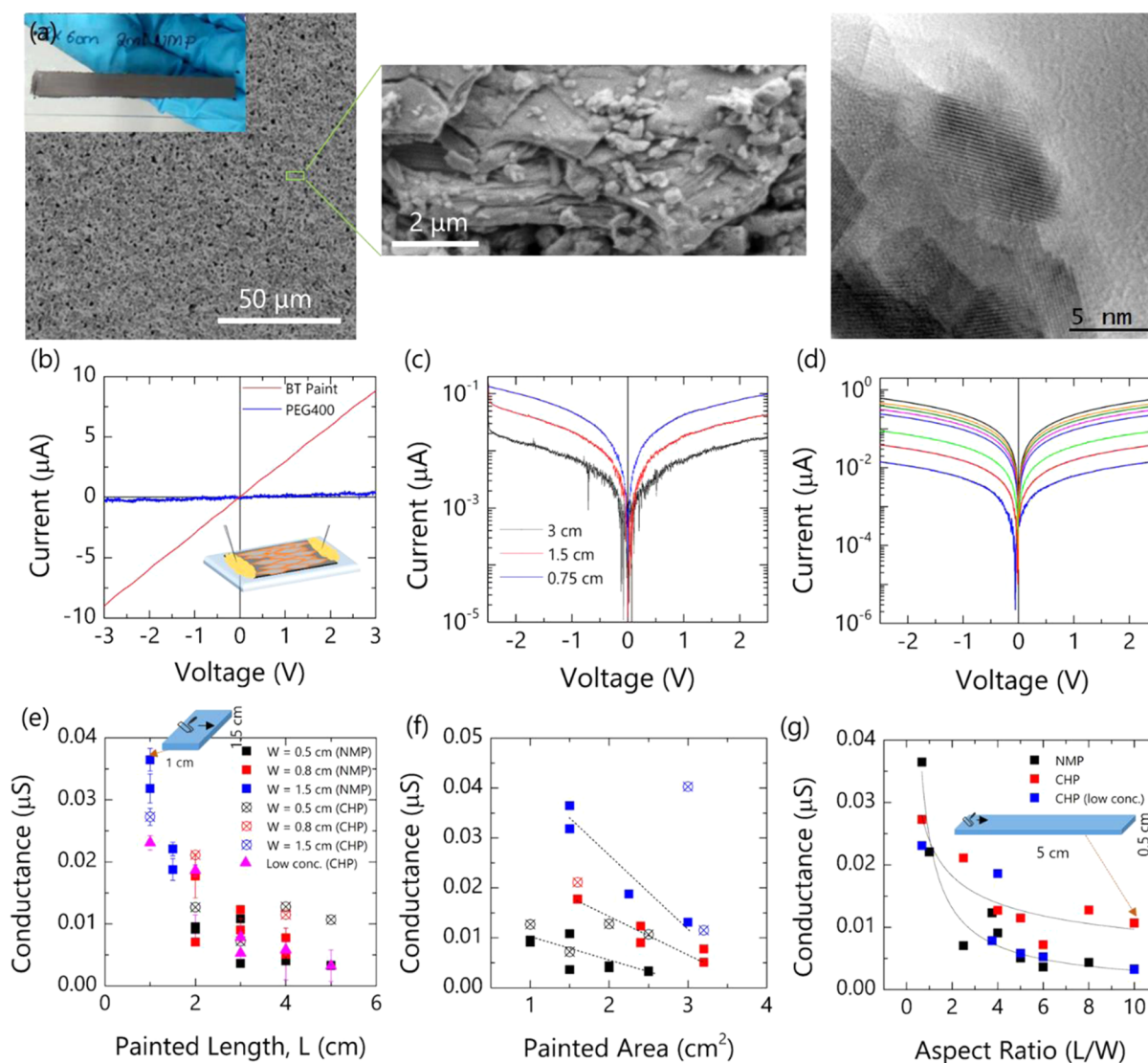


**Figure 5.** (a) Plan-view SEM, cross-sectional SEM, and HRTEM images of the 2D  $\text{Bi}_2\text{Te}_3$  paint material. (b)  $I$ - $V$  measurements showing the conductivity of the PEG vs a  $\text{Bi}_2\text{Te}_3$ -PEG paint. (c)  $I$ - $V$  plot showing the change in conductivity with different lengths and a nonzero current when crossing  $V = 0$ . (d)  $I$ - $V$  curves from individual paint strips at different lengths ranging from 0.5–3 cm. (e) Conductivity ( $I$ - $V$ ) variation as a function of length, (f) total area, and (g) aspect ratio for 2D  $\text{Bi}_2\text{Te}_3$  paints.

thickness, the contacts to other nanosheets are separated by the PEG coating (the radius of gyration of the PEG400 is under 1 nm and can easily infiltrate the nanosheet matrix when exfoliated in NMP). Figure S7 demonstrates that, at the high concentration, paints exfoliated in CHP are lower in overall conductance versus painted area compared to 2D nanosheet paint exfoliated from NMP. In Figure S8, the conductance values from  $\text{Bi}_2\text{Te}_3$  paints exfoliation in CHP are higher (typical  $\times 2$  more conductive) at lower ( $1 \text{ kg dm}^{-3}$ )  $\text{Bi}_2\text{Te}_3$  concentration. We observe little dependence of conductance on A.R. at the lower concentration for similar paint thickness. The clumpier paint from exfoliation in CHP reduced grain boundary contacts from high-density 2D grain boundaries and increased conductance overall, but the sensitive dependence on painting direction and A.R. requires the higher (same as NMP) concentration of  $\text{Bi}_2\text{Te}_3$ . We believe this effect is due to  $\text{Bi}_2\text{Te}_3$  nanosheets in 2D of few QL form that undergo directional shearing during painting.

In Figure 5(c), we show measurements of ohmic conduction from a single painted strip (NMP exfoliation, 2D) at full length

and at two point contacts of shorter distances. Current flow is measured along the direction of painting, and the conductivity increases with shorter nominal path length consistent with Matthiessen-like resistivity along a transmission line. In Figure 5(d), the  $I$ - $V$  data from a range of separate, individual paint strips of various lengths are measured, and the data show that shorter strips (all with the same width) are more conductive. Note, EELS data confirmed that the PEG is not intercalated in the van der Waals spacing between quintuple molecular thick layers and resides on the outer edges, and as such is not believed to be involved in any considerable host-guest charge transfer interactions between the basal planes of  $\text{Bi}_2\text{Te}_3$  nanosheets. Any charge trapping by the glass surface is a background and maintained in the overall conductance analysis. The use of a nonconducting polymer that was soluble in NMP was chosen so that the effect of painting and 2D sheet shearing and stacking on strips of various A.R.s could be examined.

Estimates of conductivity variation with the length of the 2D nanosheet paint are shown in Figure 5(e) for a series of

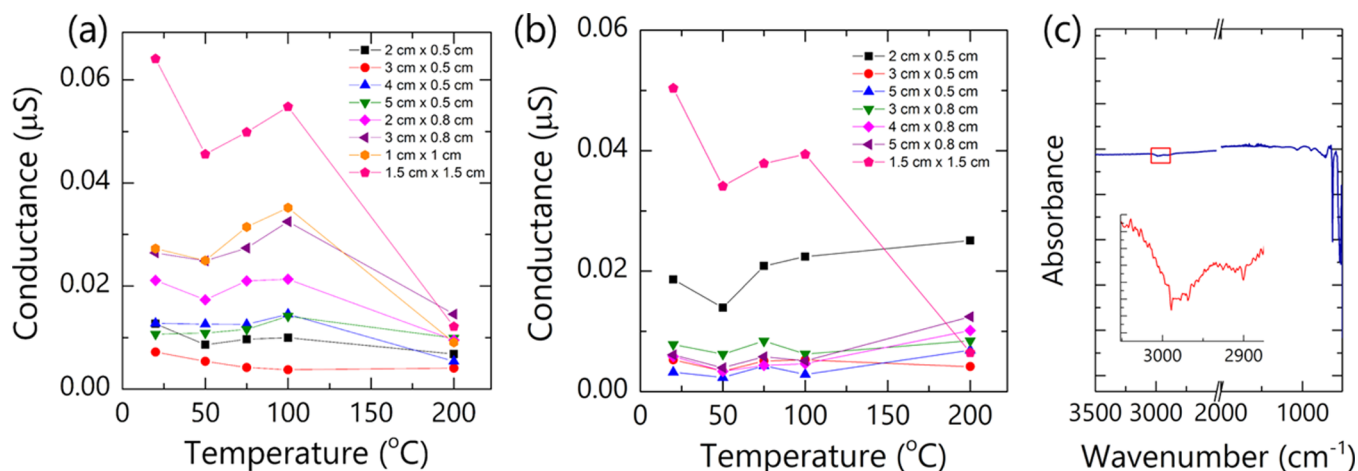


**Figure 6.** Conductance measured from individual  $I$ - $V$  measurements on 2D  $\text{Bi}_2\text{Te}_3$  nanosheet paints exfoliated in CHP and PEG with a range of A.R.'s from 1 cm  $\times$  1 to 5 cm  $\times$  0.5 cm with nominal  $\text{Bi}_2\text{Te}_3$  concentrations of (a) 4 kg  $\text{dm}^{-3}$  and (b) 1 kg  $\text{dm}^{-3}$ . (c) ATR-FTIR spectrum of the  $\text{Bi}_2\text{Te}_3$  paint after heating. Remnant low-intensity  $-\text{CH}_2/-\text{CH}_3$  vibrational modes (inset) are found, but the primary PEG signature is thermally decomposed. The low-frequency vibrations are of Bi-Te.

individually painted strips of different widths, with exfoliation in both NMP and CHP and also in CHP at the lower  $\text{Bi}_2\text{Te}_3$  concentration. The conductance values for  $I$ - $V$  curves follow a clear reduction with longer paint strips (the best fit is a power law), measured along the direction of paint application in all cases. Conductance suppression is also consistent for all paint strips as a function of the total area, when measured parallel to the direction of painting (Figure 5(f)). When scaled as a function of A.R., the trend is similar to the painted length dependence. A power law reduction on conductance ( $\sigma \sim 0.002/\sqrt{[A.R.]}$  and  $\sigma \sim 0.002/[A.R.]$  for CHP and NMP exfoliation nanosheet paints, respectively) is characteristically found for all similarly thick paint strips. The measurements do confirm the effect of painting direction on the dispersion of the 2D material on the surface. At low A.R.'s, conductance is improved by a factor of 2–4 $\times$ . For our investigations of the highest conductivity, square (A.R. = 1 or those with lower A.R.), we discovered that the conductivity both parallel and perpendicular to the painting direction is similar. For an A.R. = 1 (1.5 cm  $\times$  1.5 cm), the conductance is similar in both directions (parallel and perpendicular to the painting direction) for standard thickness and for thinner paint strips; the latter exhibit lower conductance, shown in Figure S9. This observation is consistent with length, area, and A.R. dependence shown in Figure 5(e–g). At A.R. < 1, the highest conductance is perpendicular to the painting direction, yet the highest of any A.R. paint strip is for shorter strips of similar width.

Finally, we examined the stability of these paints as a function of temperature.  $\text{Bi}_2\text{Te}_3$  has a low melting temperature close to 580  $^\circ\text{C}$  in bulk form and likely undergoes a melting point suppression in 2D form, which has implications for thermoelectric applications and the surface transport properties of topological insulators. The thermogravimetric analysis in Figure S10 confirms PEG decomposition without associated mass loss. Thermal activation of conductance mechanisms (barrier penetration to polaron hopping), and the stability of the surrounding polymer that facilitates a paint, are also important to examine.

Mo et al. also show that reducing the thickness of ultrathin  $\text{Bi}_2\text{Te}_3$  films (to 8 nm, still thicker than 2D or few QL exfoliated

films) invokes a dominant role of two-dimensional surface conduction in this material.<sup>63</sup> Those films were placed onto substrates and exhibited a defined sheet–substrate interaction that influenced conduction at the  $\text{Bi}_2\text{Te}_3$  contact surface and did not contain polymeric surface coatings. Figure 6 shows the temperature dependence of conductance for paints of all lengths, widths, and A.R.'s examined in this work (NMP exfoliation, 4 kg  $\text{dm}^{-3}$   $\text{Bi}_2\text{Te}_3$ ). Notably, paints with high A.R. and narrow (0.5 cm) widths maintain relatively stable conductance from room temperature to 200  $^\circ\text{C}$ , implying limited thermal effect on the PEG coating and nanosheet contact along the painting direction. As the A.R. was decreased, the paint conductance reduced with higher temperatures. We find a rather unique trend that square paint conductivity along the painting direction is most affected (suppressed by a factor of 3–6 $\times$ ) by higher temperatures up to 200  $^\circ\text{C}$ . The trend is clearly dependent on length and aspect ratio at the same nanosheet density and film thickness. Modifications to the PEG coating (melting) would be expected to influence the overall conductivity and nanosheet-to-nanosheet contacts, especially if carbonized. The upper temperature prevents graphitization of the polymeric carbon, yet no clear variation of conductance is found for higher aspect ratios of narrow 2D nanosheet paints.

The direction of the applied paint possibly orients the nanosheet stacks for suppressed conductance in the paint direction. Since longer painted strips increase the overall net resistance, it is ascribed to an increase in grain boundary contacts sheared by unidirectional painting application. Preferential orientation of 2D sheets of approximately similar morphology in one particular direction is similar to an isospatial distribution of filler material, where that material itself has an A.R. (e.g., tubes or fibers). At such high fill fractions used in our paint, this observation was unexpected. 2D nanosheet paints with greater overall area are more conductive if the painted width (perpendicular to the path of the applied voltage) causes an overall painted A.R. < 1.

In a restacked layered assembly via mixing with a nonconducting polymer, the electronic transport is efficient along the layers but limited in the perpendicular direction.<sup>64</sup> Grain boundaries also form intergrain contacts, increasing the overall resistivity as a function of length. While polymer located between the grains of restacked and few-layer 2D sheets

aggregates and is also nonconductive, it must facilitate intergrain contacts to maintain end-to-end conductivity through the painted film—our results demonstrate that increasing the conductivity of the painted 2D sheet composite requires a wider (short along the paint direction) painted strip. Carrier scattering and grain-boundary barriers are distributed throughout the composite, separated by porous regions.<sup>65</sup>

2D nanosheets of semiconductors mimic quantum wells with a high potential barrier, and in the Bi<sub>2</sub>Te<sub>3</sub> paint, restacked sheets in a nonconducting polymer composite matrix force a percolating current through the layer, and through the polymer connections between grains, the percolation threshold is likely minimum at very high fill fractions such as our paint. Typically, this threshold follows  $\sigma = \sigma_0(V_f - V_p)^\alpha$ , where  $V_p$  is the percolation threshold fill fraction and the exponent typically ranges from 0.5 to 2 (for 3D transport) and  $\sigma_0$  approximates the innate conductivity of the filler materials,<sup>66</sup> i.e. Bi<sub>2</sub>Te<sub>3</sub> in bulk or nanoscale form. Our fill fractions are close to 100%; PEG is the coating of the nanosheets and few-layer sheets throughout, and the percolation threshold is ill-defined. Rather, we propose the threshold discussed below is a function of a tortuous current path through the 2D Bi<sub>2</sub>Te<sub>3</sub> sheet<sup>67–70</sup> grain contacts along the minimum resistivity path. The presence of PEG between the contact ends of encapsulated few-layer nanosheet grains may also contribute to the internal resistance.

In porous conductive materials, pores that scatter charge carriers can do so by a distribution of potential perturbations and localized electric field enhancement, but the effect porous scattering is less pronounced for pores interspersed in a granular network. The total resistivity includes contributions from the material, pores, impurities, nonconductive barriers such as the PEG coating, and, of course, grain boundaries, linearly summed according to  $\rho_T = \rho_{\text{bulk}} + \rho_{\text{imp}} + \rho_{\text{pore}} + \rho_{\text{grain}} + \rho_{\text{poly}} + \dots$ . In addition to the intrinsic conductivity of Bi<sub>2</sub>Te<sub>3</sub> in 2D or few QL form<sup>71</sup> measured in experiments, the grain-boundary and pore contributions to resistivity are controlled by painting and by the density of 2D vs clumps of the material throughout the painted film. Grain boundary contacts are similar in all directions, comprising overlapping 2D and few QL materials coated with PEG. Wide paint strips provide conduction paths around pores that were shown to maximize conductance especially in cases where the length is the smallest. This supposes that short strips along the paint direction at a given width (that is less than the length) are not the best way to enhance conductivity in Bi<sub>3</sub>Te<sub>3</sub> 2D nanosheet paints of high-volume fill fraction, and likely are the case for other 2D materials that are not as conductive as graphene. Instead, to increase conductivity along the short length direction, the 2D nanosheet paint strip can be made wider for a constant thickness.

This work proposes a facile method of Bi<sub>2</sub>Te<sub>3</sub> exfoliated to 2D or few QL dimensions in NMP and CHP solvents, with direct coating by PEG, while maintaining a stable solution as an ink. The 2D nanosheet suspension ink was shown to be a conductive paint. This deposition method allows a 2D material to be painted on a wide range of surfaces and substrates. The solution-phase approach is scalable and versatile for application to a range of substrate and device constructs as a paint, and the polymer portion of the composite is minimal, added to solution directly to coat the 2D materials. The possibility of adding alternative conducting polymers and conductive additives and the use of flexible substrates are presently being explored. Such composite may form a more stable and conductive thermo-

electric material coating of p-type and n-type analogs for use in heat producing devices for energy harvesting applications. However, the insights reported here confirm that the nature of 2D materials and efficacy of solvent exfoliation seem to influence conductance in painted films in a particular way. Prior to this, the effect of A.R. on a 2D nanosheet paint with polymer added as a coating and the solvent exfoliation state was not known, and it remains to be seen if this effect will be observable in 2D composite of more conductive materials or with conductive polymer additives. A fundamental dependence on A.R. of 2D paints was uncovered using a nonconducting, soluble binding polymer. There are likely some implications for high-density 2D materials as filler or additives to polymers, rubbers, and other composites, and painting direction, thickness, width, and aspect ratio can influence conductance.

## ■ ASSOCIATED CONTENT

### 📄 Supporting Information

The Supporting Information is available free of charge on the ACS Publications website at DOI: [10.1021/acs.chemmater.7b02321](https://doi.org/10.1021/acs.chemmater.7b02321).

Additional characterization of film thickness by AFM, optical images of painted Bi<sub>2</sub>Te<sub>3</sub> strips, SEM characterization, electrical conductance data, thermogravimetric analysis of painted strips, electron diffraction data of individual nanosheets, and background subtraction of low-loss EELS spectra (PDF)

## ■ AUTHOR INFORMATION

### Corresponding Author

\*E-mail: [c.odwyer@ucc.ie](mailto:c.odwyer@ucc.ie), Tel: +353 21 490 2732.

### ORCID

Justin D. Holmes: [0000-0001-5087-8936](https://orcid.org/0000-0001-5087-8936)

Kafil M. Razeed: [0000-0001-9360-9277](https://orcid.org/0000-0001-9360-9277)

Colm O'Dwyer: [0000-0001-7429-015X](https://orcid.org/0000-0001-7429-015X)

### Notes

The authors declare no competing financial interest.

## ■ ACKNOWLEDGMENTS

E.C. and C.O'D. acknowledge the support of the Irish Research Council (IRC) Enterprise Partnership Scheme with Analog Devices B.V. under award EPSPG/2011/160. D.B. acknowledges support from IRC Government of Ireland Postgraduate Award under contract GOIPG/2014/206. This work was also supported by Science Foundation Ireland (SFI) under the National Access Programme (NAP 417). C.O'D. acknowledges support by SFI through SFI Technology Innovation and Development Awards under contract nos 13/TIDA/E2761 and 15/TIDA/2893. G.C. acknowledges support from and Irish Research Council New Foundations Award. M.S.M. acknowledges CONICET and ANPCyT PICT 2012-1136 (Argentina). N.V.V.M. thanks LNNano-CNPEM (Campinas, Brazil), which is supported by Brazilian Ministry of Science, Technology, Innovation and Communication (MCTIC), for the usage of TEM facilities. K.M.R. acknowledges funding from the European Union's Horizon2020 funded project "Thermally Integrated Smart Photonics Systems (TIPS)", under grant agreement No. 644453. This publication has also emanated from research supported in part by a research grant from SFI under Grant Number 14/IA/2581.

## REFERENCES

- (1) Poudel, B.; Hao, Q.; Ma, Y.; Lan, Y.; Minnich, A.; Yu, B.; Yan, X.; Wang, D.; Muto, A.; Vashaev, D.; Chen, X.; Liu, J.; Dresselhaus, M. S.; Chen, G.; Ren, Z. High-Thermoelectric Performance of Nanostructured Bismuth Antimony Telluride Bulk Alloys. *Science* **2008**, *320*, 634–638.
- (2) Coleman, J. N.; Lotya, M.; O'Neill, A.; Bergin, S. D.; King, P. J.; Khan, U.; Young, K.; Gaucher, A.; De, S.; Smith, R. J.; Shvets, I. V.; Arora, S. K.; Stanton, G.; Kim, H.-Y.; Lee, K.; Kim, G. T.; Duesberg, G. S.; Hallam, T.; Boland, J. J.; Wang, J. J.; Donegan, J. F.; Grunlan, J. C.; Moriarty, G.; Shmeliov, A.; Nicholls, R. J.; Perkins, J. M.; Grievson, E. M.; Theuwissen, K.; McComb, D. W.; Nellist, P. D.; Nicolosi, V. Two-Dimensional Nanosheets Produced by Liquid Exfoliation of Layered Materials. *Science* **2011**, *331*, 568–571.
- (3) Nicolosi, V.; Chhowalla, M.; Kanatzidis, M. G.; Strano, M. S.; Coleman, J. N. Liquid Exfoliation of Layered Materials. *Science* **2013**, *340*, 1226419.
- (4) Ghidui, M.; Lukatskaya, M. R.; Zhao, M.-Q.; Gogotsi, Y.; Barsoum, M. W. Conductive Two-dimensional Titanium Carbide 'Clay' with High Volumetric Capacitance. *Nature* **2014**, *516*, 78–81.
- (5) Lukatskaya, M. R.; Mashtalir, O.; Ren, C. E.; Dall'Agnese, Y.; Rozier, P.; Taberna, P. L.; Naguib, M.; Simon, P.; Barsoum, M. W.; Gogotsi, Y. Cation Intercalation and High Volumetric Capacitance of Two-Dimensional Titanium Carbide. *Science* **2013**, *341*, 1502–1505.
- (6) Boland, C. S.; Khan, U.; Ryan, G.; Barwich, S.; Charifou, R.; Harvey, A.; Backes, C.; Li, Z.; Ferreira, M. S.; Möbius, M. E.; Young, R. J.; Coleman, J. N. Sensitive Electrochemical Sensors using Viscoelastic Graphene-Polymer Nanocomposites. *Science* **2016**, *354*, 1257–1260.
- (7) Chowdhury, I.; Prasher, R.; Lofgreen, K.; Chrysler, G.; Narasimhan, S.; Mahajan, R.; Koester, D.; Alley, R.; Venkatasubramanian, R. On-Chip Cooling by Superlattice-Based Thin-Film Thermoelectrics. *Nat. Nanotechnol.* **2009**, *4*, 235–238.
- (8) Majumdar, A. Thermoelectric Devices: Helping Chips to Keep their Cool. *Nat. Nanotechnol.* **2009**, *4*, 214–215.
- (9) Majumdar, A. Thermoelectricity in Semiconductor Nanostructures. *Science* **2004**, *303*, 777–778.
- (10) Venkatasubramanian, R.; Siivola, E.; Colpitts, T.; O'Quinn, B. Thin-Film Thermoelectric Devices with High Room-Temperature Figures of Merit. *Nature* **2001**, *413*, 597–602.
- (11) Harman, T. C.; Taylor, P. J.; Walsh, M. P.; LaForge, B. E. Quantum Dot Superlattice Thermoelectric Materials and Devices. *Science* **2002**, *297*, 2229–2232.
- (12) Zhang, H.; Liu, C.-X.; Dai, X.; Fang, Z.; Zhang, S.-C. Topological Insulators in  $\text{Bi}_2\text{Se}_3$ ,  $\text{Bi}_2\text{Te}_3$  and  $\text{Sb}_2\text{Te}_3$  with a Single Dirac Cone on the Surface. *Nat. Phys.* **2009**, *5*, 438–442.
- (13) Hasan, M. Z.; Kane, C. L. Topological Insulators. *Rev. Mod. Phys.* **2010**, *82*, 3045–3067.
- (14) Stavila, V.; Robinson, D. B.; Hekmaty, M. A.; Nishimoto, R.; Medlin, D. L.; Zhu, S.; Tritt, T. M.; Sharma, P. A. Wet-Chemical Synthesis and Consolidation of Stoichiometric Bismuth Telluride Nanoparticles for Improving the Thermoelectric Figure-of-Merit. *ACS Appl. Mater. Interfaces* **2013**, *5*, 6678–6686.
- (15) Shahil, K. M. F.; Hossain, M. Z.; Teweldebrhan, D.; Balandin, A. A. Crystal Symmetry Breaking in Few-Quintuple  $\text{Bi}_2\text{Te}_3$  Films: Applications in Nanometrology of Topological Insulators. *Appl. Phys. Lett.* **2010**, *96*, 153103.
- (16) Saleemi, M.; Toprak, M. S.; Li, S.; Johnsson, M.; Muhammed, M. Synthesis, processing, and thermoelectric properties of bulk nanostructured bismuth telluride ( $\text{Bi}_2\text{Te}_3$ ). *J. Mater. Chem.* **2012**, *22*, 725–730.
- (17) Mishra, S. K.; Satpathy, S.; Jepsen, O. Electronic Structure and Thermoelectric Properties of Bismuth Telluride and Bismuth Selenide. *J. Phys.: Condens. Matter* **1997**, *9*, 461–470.
- (18) Hicks, L. D.; Dresselhaus, M. S. Effect of Quantum-Well Structures on the Thermoelectric Figure of Merit. *Phys. Rev. B: Condens. Matter Mater. Phys.* **1993**, *47*, 12727–12731.
- (19) O'Dwyer, M. F.; Humphrey, T. E.; Linke, H. Concept Study for a High-Efficiency Nanowire Based Thermoelectric. *Nanotechnology* **2006**, *17*, S338–S343.
- (20) Kim, S. I.; Lee, K. H.; Mun, H. A.; Kim, H. S.; Hwang, S. W.; Roh, J. W.; Yang, D. J.; Shin, W. H.; Li, X. S.; Lee, Y. H.; Snyder, G. J.; Kim, S. W. Dense Dislocation Arrays Embedded in Grain Boundaries for High-Performance Bulk Thermoelectrics. *Science* **2015**, *348*, 109–114.
- (21) Sarnet, T.; Hatanpää, T.; Puukilainen, E.; Mattinen, M.; Vehkamäki, M.; Mizohata, K.; Ritala, M.; Leskelä, M. Atomic Layer Deposition and Characterization of  $\text{Bi}_2\text{Te}_3$  Thin Films. *J. Phys. Chem. A* **2015**, *119*, 2298–2306.
- (22) Hansen, A.-L.; Dankwort, T.; Winkler, M.; Ditto, J.; Johnson, D. C.; Koenig, J. D.; Bartholomé, K.; Kienle, L.; Bensch, W. Synthesis and Thermal Instability of High-Quality  $\text{Bi}_2\text{Te}_3/\text{Sb}_2\text{Te}_3$  Superlattice Thin Film Thermoelectrics. *Chem. Mater.* **2014**, *26*, 6518–6522.
- (23) Liang, L.-X.; Deng, Y.; Wang, Y.; Gao, H.-L.; Cui, J. Scalable solution assembly of nanosheets into high-performance flexible  $\text{Bi}_{0.5}\text{Sb}_{1.5}\text{Te}_3$  thin films for thermoelectric energy conversion. *J. Nanopart. Res.* **2014**, *16*, 2575–2582.
- (24) Takashiri, M.; Tanaka, S.; Miyazaki, K. Determination of the Origin of Crystal Orientation for Nanocrystalline Bismuth Telluride-Based Thin Films Prepared by Use of the Flash Evaporation Method. *J. Electron. Mater.* **2014**, *43*, 1881–1889.
- (25) Geim, A. K.; Novoselov, K. S. The rise of graphene. *Nat. Mater.* **2007**, *6*, 183–191.
- (26) Novoselov, K. S.; Geim, A. K.; Morozov, S. V.; Jiang, D.; Katsnelson, M. I.; Grigorieva, I. V.; Dubonos, S. V.; Firsov, A. A. Two-Dimensional Gas of Massless Dirac Fermions in Graphene. *Nature* **2005**, *438*, 197–200.
- (27) Novoselov, K. S.; Geim, A. K.; Morozov, S. V.; Jiang, D.; Zhang, Y.; Dubonos, S. V.; Grigorieva, I. V.; Firsov, A. A. Electric Field Effect in Atomically Thin Carbon Films. *Science* **2004**, *306*, 666–669.
- (28) Zou, H.; Rowe, D. M.; Min, G. Growth of p- and n-type Bismuth Telluride Thin Films by Co-Evaporation. *J. Cryst. Growth* **2001**, *222*, 82–87.
- (29) Kim, D.-H.; Byon, E.; Lee, G.-H.; Cho, S. Effect of Deposition Temperature on the Structural and Thermoelectric Properties of Bismuth Telluride Thin Films Grown by Co-Sputtering. *Thin Solid Films* **2006**, *510*, 148–153.
- (30) Li, S.; Toprak, M. S.; Soliman, H. M. A.; Zhou, J.; Muhammed, M.; Platzek, D.; Müller, E. Fabrication of Nanostructured Thermoelectric Bismuth Telluride Thick Films by Electrochemical Deposition. *Chem. Mater.* **2006**, *18*, 3627–3633.
- (31) Hernandez, Y.; Nicolosi, V.; Lotya, M.; Blighe, F. M.; Sun, Z.; De, S.; McGovern, I. T.; Holland, B.; Byrne, M.; Gun'Ko, Y. K.; Boland, J. J.; Niraj, P.; Duesberg, G.; Krishnamurthy, S.; Goodhue, R.; Hutchison, J.; Scardaci, V.; Ferrari, A. C.; Coleman, J. N. High-Yield Production of Graphene by Liquid-Phase Exfoliation of Graphite. *Nat. Nanotechnol.* **2008**, *3*, 563–568.
- (32) Chhowalla, M.; Shin, H. S.; Eda, G.; Li, L.-J.; Loh, K. P.; Zhang, H. The Chemistry of Two-Dimensional Layered Transition Metal Dichalcogenide Nanosheets. *Nat. Chem.* **2013**, *5*, 263–275.
- (33) Geim, A. K. Graphene: Status and Prospects. *Science* **2009**, *324*, 1530–1534.
- (34) Kim, Y.; Zhu, J.; Yeom, B.; Di Prima, M.; Su, X.; Kim, J.-G.; Yoo, S. J.; Uher, C.; Kotov, N. A. Stretchable Nanoparticle Conductors with Self-Organized Conductive Pathways. *Nature* **2013**, *500*, 59–63.
- (35) Du, Y.; Shen, S. Z.; Cai, K.; Casey, P. S. Research Progress on Polymer-Inorganic Thermoelectric Nanocomposite Materials. *Prog. Polym. Sci.* **2012**, *37*, 820–841.
- (36) Park, S. H.; Jo, S.; Kwon, B.; Kim, F.; Ban, H. W.; Lee, J. E.; Gu, D. H.; Lee, S. H.; Hwang, Y.; Kim, J.-S.; Hyun, D.-B.; Lee, S.; Choi, K. J.; Jo, W.; Son, J. S. High-Performance Shape-Engineerable Thermoelectric Painting. *Nat. Commun.* **2016**, *7*, 13403.
- (37) Austin, I. G. The Optical Properties of Bismuth Telluride. *Proc. Phys. Soc., London* **1958**, *72*, 545.

- (38) Basile, G.; Bernardin, C.; Olla, S. Momentum Conserving Model with Anomalous Thermal Conductivity in Low Dimensional Systems. *Phys. Rev. Lett.* **2006**, *96*, 204303.
- (39) Bauer, S.; Bobisch, C. A. Nanoscale Electron Transport at the Surface of a Topological Insulator. *Nat. Commun.* **2016**, *7*, 11381.
- (40) Diaz, C.; Lavayen, V.; O'Dwyer, C. Single-crystal Micro/nanostructures and Thin Films of Lamellar Molybdenum Oxide by Solid-state Pyrolysis of Organometallic Derivatives of a Cyclo-triphosphazene. *J. Solid State Chem.* **2010**, *183*, 1595–1603.
- (41) He, R.; Chung, T.-F.; Delaney, C.; Keiser, C.; Jauregui, L. A.; Shand, P. M.; Chancey, C. C.; Wang, Y.; Bao, J.; Chen, Y. P. Observation of Low Energy Raman Modes in Twisted Bilayer Graphene. *Nano Lett.* **2013**, *13*, 3594–3601.
- (42) He, R.; Sucharitakul, S.; Ye, Z.; Keiser, C.; Kidd, T.; Gao, X. P. A. Laser Induced Oxidation and Optical Properties of Stoichiometric and Non-Stoichiometric Bi<sub>2</sub>Te<sub>3</sub> Nanoplates. *Nano Res.* **2015**, *8*, 851–859.
- (43) Thripuranthaka, M.; Kashid, R. V.; Sekhar Rout, C.; Late, D. J. Temperature Dependent Raman Spectroscopy of Chemically Derived Few Layer MoS<sub>2</sub> and WS<sub>2</sub> Nanosheets. *Appl. Phys. Lett.* **2014**, *104*, 081911.
- (44) Berkdemir, A.; Gutiérrez, H. R.; Botello-Méndez, A. R.; Perea-López, N.; Elías, A. L.; Chia, C.-I.; Wang, B.; Crespi, V. H.; López-Urías, F.; Charlier, J.-C.; Terrones, H.; Terrones, M. Identification of Individual and Few Layers of WS<sub>2</sub> using Raman Spectroscopy. *Sci. Rep.* **2013**, *3*, 1755.
- (45) Teweldebrhan, D.; Goyal, V.; Rahman, M.; Balandin, A. A. Atomically-thin crystalline films and ribbons of bismuth telluride. *Appl. Phys. Lett.* **2010**, *96*, 053107.
- (46) Terrones, H.; Corro, E. D.; Feng, S.; Poumirol, J. M.; Rhodes, D.; Smirnov, D.; Pradhan, N. R.; Lin, Z.; Nguyen, M. A. T.; Elías, A. L.; Mallouk, T. E.; Balicas, L.; Pimenta, M. A.; Terrones, M. New First Order Raman-active Modes in Few Layered Transition Metal Dichalcogenides. *Sci. Rep.* **2015**, *4*, 4215.
- (47) Mak, K. F.; He, K.; Shan, J.; Heinz, T. F. Control of Valley Polarization in Monolayer MoS<sub>2</sub> by Optical Helicity. *Nat. Nanotechnol.* **2012**, *7*, 494–498.
- (48) Shahil, K. M. F.; Hossain, M. Z.; Teweldebrhan, D.; Balandin, A. A. Crystal Symmetry Breaking in Few-Quintuple Bi<sub>2</sub>Te<sub>3</sub> Films: Applications in Nanometrology of Topological Insulators. *Appl. Phys. Lett.* **2010**, *96*, 153103.
- (49) He, R.; Wang, Z.; Qiu, R. L. J.; Delaney, C.; Beck, B.; Kidd, T. E.; Chancey, C. C.; Gao, X. P. A. Observation of Infrared-Active Modes in Raman Scattering from Topological Insulator Nanoplates. *Nanotechnology* **2012**, *23*, 455703.
- (50) Liang, Y. J.; Wang, W. Z.; Zeng, B. Q.; Zhang, G. L.; Song, Y. Y.; Zhang, X. Y.; Huang, J.; Li, J.; Li, T. The Effect of the Bi Source on Optical Properties of Bi<sub>2</sub>Te<sub>3</sub> Nanostructures. *Solid State Commun.* **2011**, *151*, 704–707.
- (51) Song, W.-L.; Cao, M.-S.; Lu, M.-M.; Bi, S.; Wang, C.-Y.; Liu, J.; Yuan, J.; Fan, L.-Z. Flexible Graphene/Polymer Composite Films in Sandwich Structures for Effective Electromagnetic Interference Shielding. *Carbon* **2014**, *66*, 67–76.
- (52) Noël, A.; Faucheu, J.; Rieu, M.; Viricelle, J.-P.; Bourgeat-Lami, E. Tunable Architecture for Flexible and Highly Conductive Graphene-Polymer Composites. *Compos. Sci. Technol.* **2014**, *95*, 82–88.
- (53) Heeder, N.; Yussuf, A.; Chakraborty, I.; Godfrin, M. P.; Hurt, R.; Tripathi, A.; Bose, A.; Shukla, A. Fixed-angle rotary shear as a new method for tailoring electro-mechanical properties of templated graphene-polymer composites. *Compos. Sci. Technol.* **2014**, *100*, 70–75.
- (54) Lee, J. S.; Ko, Y. S. Synthesis of Petaloid Graphene/Polyethylene Composite Nanosheet Produced by Ethylene Polymerization with Metallocene Catalyst Adsorbed on Multilayer Graphene. *Catal. Today* **2014**, *232*, 82–88.
- (55) Gannon, G.; O'Dwyer, C.; Larsson, J. A.; Thompson, D. Interdigitating Organic Bilayers Direct the Short Interlayer Spacing in Hybrid Organic-Inorganic Layered Vanadium Oxide Nanostructures. *J. Phys. Chem. B* **2011**, *115*, 14518–14525.
- (56) O'Dwyer, C.; Gannon, G.; McNulty, D.; Buckley, D. N.; Thompson, D. Accommodating Curvature in a Highly Ordered Functionalized Metal Oxide Nanofiber: Synthesis, Characterization, and Multiscale Modeling of Layered Nanosheets. *Chem. Mater.* **2012**, *24*, 3981–3992.
- (57) Wu, C. G.; DeGroot, D. C.; Marcy, H. O.; Schindler, J. L.; Kannewurf, C. R.; Liu, Y. J.; Hirpo, W.; Kanatzidis, M. G. Redox Intercalative Polymerization of Aniline in V<sub>2</sub>O<sub>5</sub> Xerogel. The Postintercalative Intralamellar Polymer Growth in Polyaniline/Metal Oxide Nanocomposites Is Facilitated by Molecular Oxygen. *Chem. Mater.* **1996**, *8*, 1992–2004.
- (58) Petkov, V.; Parvanov, V.; Trikalitis, P.; Malliakas, C.; Vogt, T.; Kanatzidis, M. G. Three-Dimensional Structure of Nanocomposites from Atomic Pair Distribution Function Analysis: Study of Polyaniline and (Polyaniline)<sub>0.5</sub>V<sub>2</sub>O<sub>5</sub>·1.0H<sub>2</sub>O. *J. Am. Chem. Soc.* **2005**, *127*, 8805–8812.
- (59) Jiang, S.; Li, Z.; Huang, S.; Lu, S.; Yu, Y.; Mou, G.; Xu, J.; Zhu, Q.; Tan, X.; Zhu, X.; Zakharaova, G. S. Synthesis and Electrochromic Characterization of the Graphene/Poly(ethylene oxide)/V<sub>2</sub>O<sub>5</sub>·nH<sub>2</sub>O Ternary Nanocomposite Films. *J. Electrochem. Soc.* **2014**, *161*, H684–H688.
- (60) Tsen, A. W.; Brown, L.; Levendorf, M. P.; Ghahari, F.; Huang, P. Y.; Havener, R. W.; Ruiz-Vargas, C. S.; Muller, D. A.; Kim, P.; Park, J. Tailoring Electrical Transport Across Grain Boundaries in Polycrystalline Graphene. *Science* **2012**, *336*, 1143–1146.
- (61) Taherian, R. Development of an Equation to Model Electrical Conductivity of Polymer-Based Carbon Nanocomposites. *ECS J. Solid State Sci. Technol.* **2014**, *3*, M26–M38.
- (62) Gong, L.; Young, R. J.; Kinloch, I. A.; Riaz, I.; Jalil, R.; Novoselov, K. S. Optimizing the Reinforcement of Polymer-Based Nanocomposites by Graphene. *ACS Nano* **2012**, *6*, 2086–2095.
- (63) Mo, D. L.; Wang, W. B.; Cai, Q. Influence of Thickness on the Electrical Transport Properties of Exfoliated Bi<sub>2</sub>Te<sub>3</sub>. *Nanoscale Res. Lett.* **2016**, *11*, 354–362.
- (64) Glynn, C.; Thompson, D.; Paez, J.; Collins, G.; Benavente, E.; Lavayen, V.; Yutronic, N.; Holmes, J. D.; Gonzalez, G.; O'Dwyer, C. Large Directional Conductivity Change in Chemically Stable Layered Thin Films of Vanadium Oxide and a 1D Metal Complex. *J. Mater. Chem. C* **2013**, *1*, 5675–5684.
- (65) Lee, H.; Vashae, D.; Wang, D. Z.; Dresselhaus, M. S.; Ren, Z. F.; Chen, G. Effects of Nanoscale Porosity on Thermoelectric Properties of SiGe. *J. Appl. Phys.* **2010**, *107*, 094308.
- (66) May, P.; Khan, U.; O'Neill, A.; Coleman, J. N. Approaching the Theoretical Limit for Reinforcing Polymers with Graphene. *J. Mater. Chem.* **2012**, *22*, 1278–1282.
- (67) Coleman, J. N.; Curran, S.; Dalton, A. B.; Davey, A. P.; McCarthy, B.; Blau, W.; Barklie, R. C. Percolation-Dominated Conductivity in a Conjugated-Polymer-Carbon-Nanotube Composite. *Phys. Rev. B: Condens. Matter Phys.* **1998**, *58*, R7492–R7495.
- (68) De, S.; King, P. J.; Lyons, P. E.; Khan, U.; Coleman, J. N. Size Effects and the Problem with Percolation in Nanostructured Transparent Conductors. *ACS Nano* **2010**, *4*, 7064–7072.
- (69) De, S.; Coleman, J. N. Are There Fundamental Limitations on the Sheet Resistance and Transmittance of Thin Graphene Films? *ACS Nano* **2010**, *4*, 2713–2720.
- (70) Stauffer, D. Finite-Size Effect in Seven-Dimensional Site Percolation. *Phys. A* **1994**, *210*, 317–319.
- (71) Chiritescu, C.; Mortensen, C.; Cahill, D. G.; Johnson, D.; Zschack, P. Lower Limit to the Lattice Thermal Conductivity of Nanostructured Bi<sub>2</sub>Te<sub>3</sub>-Based Materials. *J. Appl. Phys.* **2009**, *106*, 073503.